Heat treatment simulation of Ti-6Al-4V parts produced by selective laser melting

Amandine Cardon [a,b,*], Charles Mareau [b], Yessine Ayed [b], Sjoerd Van Der Veen [a], Eliane Giraud [b], Philippe Dal Santo [b]

[a] Airbus Operations SAS, 316 route de Bayonne, Toulouse, France
[b] Laboratoire Angevin de Mécanique, Procédés et innovAtion, 2 Boulevard du Ronceray, Angers, France

Keywords:
SLM
Ti-6Al-4V
Heat treatment
Creep
Simulation

A B S T R A C T

The present work focuses on the simulation of the heat treatment applied after printing of Ti-6Al-4V parts. The numerical tool aims at predicting the influence of heat treatment conditions (e.g. holding time, temperature) on the residual stress field and the distortions for SLM produced parts. The numerical model relies on a thermo-viscoplastic constitutive model. To determine the corresponding material parameters, different creep tests have been performed at temperatures ranging from 723 K to 1173 K. According to the results, the stationary creep strain rate is independent of the hydrostatic pressure, which indicates that the high temperature behavior is not impacted by the initial porosity. Also, the material parameters are observed to change significantly from 873 K, which is due to the progressive transformation of the initial martensitic α' microstructure into the $\alpha+\beta$ lamellar microstructure. To validate the proposed approach, some numerical simulations have been performed for two different parts, for which distortions have been measured. The numerical and experimental distortions have then been compared to each other. For both parts, the agreement between experimental and numerical data is correct.

1. Introduction

Selective Laser Melting (SLM) is an Additive Manufacturing (AM) process that consists in selectively melting successive layers of powder with a laser. Because this process allows producing complex shaped parts, it is of great interest for industrial applications, especially those benefiting from geometrical optimization techniques. However, for some applications, the residual stresses resulting from high thermal gradients and volume changes [1] can be problematic (Fig. 1). Indeed, because residual stresses can cause distortion and have a negative impact on the fatigue behavior [2], a stress relief heat treatment is often carried out after printing operations. The global process, which includes both printing and post-printing operations, is quite difficult to apprehend, mostly because the thermo-mechanical loading conditions largely depend on geometrical and processing parameters. To understand how these parameters may impact the final properties of a component, numerical simulation is commonly used. Different studies have therefore been carried out to develop some numerical models for either the simulation of printing [3] or stress relaxation [4].

Because this aspect is essential for many industrial applications, stress relaxation in Ti-6Al-4V has been largely studied. For instance, Zong et al. [5] have investigated the short term creep and relaxation behaviors of this alloy at temperatures from 923 K to 1073 K for the sheet forming and hot-sizing processes. Liu et al. [6] have studied the creep and relaxation behaviors of Ti-6Al-4V at 973 K to simulate creep forming. Cui et al. [7] have developed an empirical equation to predict the stress relaxation from 873 K to 973 K during hot sizing. Xiao et al. [8] performed stress relaxation tests under constant temperature from 923 K to 1023 K. They have identified a constitutive model based on their relaxation tests and validated the results with the simulation of the hot stretch-creep forming of a Ti-6Al-4V sheet. Finally, Yan et al. [9] found that the stress relaxation during post welding heat treatment is correctly described by the Arrhenius power law creep model and identified the corresponding parameters for a two phase $\alpha+\beta$ microstructure.

The aforementioned experimental data is not appropriate when

* Corresponding author at: Airbus Operations SAS, 316 route de Bayonne, Toulouse, France.
E-mail addresses: amandine.cardon@ensam.eu (A. Cardon), charles.mareau@ensam.eu (C. Mareau), yessine.ayed@ensam.eu (Y. Ayed), sjoerd.van-der-veen@airbus.com (S. Van Der Veen), eliane.giraud@ensam.eu (E. Giraud), philippe.dalsanto@ensam.eu (P. Dal Santo).

https://doi.org/10.1016/j.addma.2020.101766

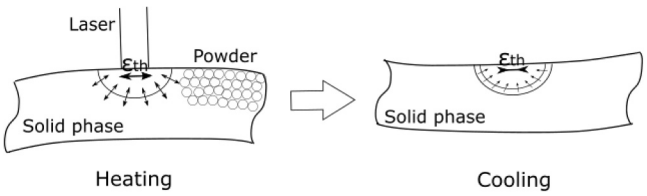

Fig. 1. Residual stress formation during SLM process.

dealing with SLM produced Ti-6Al-4V. Indeed, the microstructure of the Ti-6Al-4V alloy after SLM is quite different [10] from that obtained from conventional processes (e.g. rolling). Specifically, because of high cooling rates, the microstructure obtained after printing mostly consists of α' martensite [10], rather than the equilibrium α and β phases. As a result, there are some differences regarding stress relaxation between additively manufactured and conventionally processed Ti-6Al-4V. Specifically, Wang et al. [11] have shown that, for temperatures ranging from 873 K to 973 K, the stress relaxation rate is lower for the additively manufactured Ti-6Al-4V. This difference has been attributed to the narrow α laths obtained from the directed energy deposition process. Regarding the SLM process, Kim et al. [12] have compared the compression creep behavior of Ti-6Al-4V with as-fabricated and heat treated (1313 K for 1 h) specimens at 773 K. Results show that the Widmanstätten microstructure obtained after heat treatment has a better creep resistance than the martensitic one.

The present study aims at simulating the stress relief heat treatment applied after printing for SLM produced Ti-6Al-4V parts. This numerical tool should allow predicting the impact of heat treatment conditions (e.g. holding time, temperature) on the residual stress field and the distortions for SLM produced parts. As only little information exists on the high temperature behavior of Ti-6Al-4V with an initial martensitic microstructure, the key novelty of this work is the characterization of the mechanical behavior of this alloy at high temperature (ranging from 723 K to 1173 K). Another aspect is the identification of the material parameters of a constitutive model based on these results. This model is implemented within a Finite Element Method (FEM) solver. For validation purposes, the distortions obtained with the proposed model are finally compared to some experimental data for different parts.

2. Experimental characterization of the high temperature behavior of the Ti-6Al-4V alloy

2.1. Material description

The Ti-6Al-4V alloy is widely used in the aerospace industry because of its good properties. It has good resistance to corrosion, high specific strength, and excellent thermal resistance. In this work, this titanium alloy has been produced by SLM. After melting, the material is rapidly cooled, which leads to a fully acicular martensitic microstructure. According to the literature [13,14], this microstructure, which is shown in Fig. 2, is typical of the SLM process. Also, some spherical pores, whose ~~typical~~ diameter is about 1–10 μm, are observed after printing (Fig. 2).

According to the literature [15], mechanical properties of the SLM-produced Ti-6Al-4V alloy are possibly anisotropic. Nevertheless, when comparing the various existing data [16–18], the difference between the mechanical properties along the printing and transversal directions is comparable to the standard deviation calculated from the data given by the literature [15]. Moreover, the samples used in this study were printed with an EOS M290 and with the recommended printing parameters. According to the EOS mechanical tests results [19], the mechanical properties are not significantly impacted by the direction. As a consequence, the material is assumed to be isotropic in the following.

2.2. Creep tests

2.2.1. Tension creep tests

To evaluate the mechanical behavior of the SLM produced Ti-6Al-4V, some uniaxial creep tests under tension have been conducted at temperatures ranging from 723 K to 1173 K (450–900 °C). These tests have been performed using a Gleeble® machine with a load capacity of 100 kN. The specimen geometry is shown in Fig. 3, the specimen are as-built and polished to improve the homogeneity of the temperature. During creep tests, the axial strain has been measured with an extensometer, and an initial gauge length of 14 mm. The temperature has been controlled with a K-type thermocouple, which was placed at the center of the specimen. Prior to these tests, some preliminary tests with multiple thermocouples were conducted, to ensure that temperature gradients in the gauge region of the tension specimens are negligible. Also, creep tests have been conducted under vacuum conditions (40 Pa) to limit the oxidation. During creep tests, the axial force has been adjusted as a function of the axial elongation to keep the true axial stress σ constant. Creep tests have been stopped for an axial strain of 20%. As a consequence, the tertiary stage, which is not of interest for the present study, is not always captured during creep tests. To check repeatability, three tests have been performed for each configuration.

2.2.2. Compression creep tests

To determine whether the high temperature behavior of the SLM produced Ti-6Al-4V is dependent on the hydrostatic pressure or not, some uniaxial creep tests under compression have been performed. The

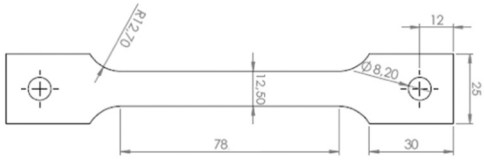

Fig. 3. Specimen geometry for tensile creep tests.

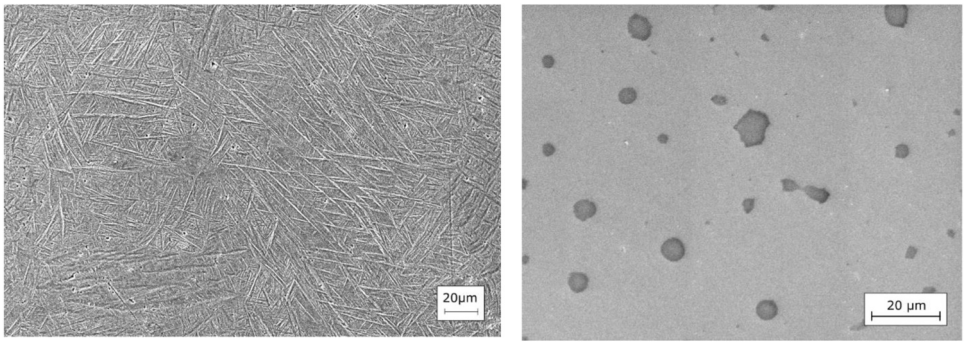

Fig. 2. Microstructure after SLM: martensitic phase (left) and porosity (right).

experimental set-up is the same as for tension tests, except that cylindrical specimens (see Fig. 4) were used instead of flat specimens. For these tests, the initial gauge length was 10 mm. The temperature field homogeneity has been verified with a preliminary test using three thermocouples, one being located in the middle and two being located at the extremities of the gauge length. After this verification, only one thermocouple located at the center of the gauge length has been used for the compressive creep tests.

2.3. Experimental procedure of the cantilever

Based on the creep tests performed at high temperatures, a constitutive model has been identified (cf. Section 3.1). Then, an experimental set up has been put in place to validate this model. In that sense, six cantilevers have been printed with an EOS M290 machine (SLM) and a Ti-6Al-4V powder. In this print, the layer size was 30 μm and the laser direction rotates with an angle of 67° from one layer to the next. After printing, the cantilevers are 110 mm long, 10 mm wide and 11 mm high (Fig. 5). These cantilevers, still attached to the baseplate, have then been split into two batches to undergo two different partial heat treatments. These two heat treatments are referred to as "partial" because they have been designed to not fully relax the residual stresses so that the cantilevers distort after being wire-cut from the baseplate. These partial heat treatments are meant to test the ability of the proposed model at predicting distortions. The first heat treatment consists of heating parts to 773 K. The parts are then held at this temperature for 1000 s and finally cooled down to room temperature. For the second heat treatment, the parts have been heated at 873 K and cooled to room temperature immediately after without any holding. Figs. 6 and 7 show the temperature evolution measured by the furnace sensor for the heat treatments 1 and 2. After being printed, heat treated and wire-cut, the six cantilevers from both batches were 3D scanned using the GOM ATOS® technology (Fig. 5), which uses a triangulation principle.

2.4. Microstructure characterization

To investigate how the microstructure evolves during a heat treatment, different samples have been heat treated at temperatures ranging from 723 K to 1173 K and holding times ranging from 20 min to 2 h. After treatment, samples were cut, polished, and etched with Kroll reagent to reveal the microstructure. Some metallographic observations have then been carried out with a Scanning Electron Microscope (SEM). The results are presented in the next section.

Moreover, some X-Ray Diffraction (XRD) analyses have also been performed to detect the formation of the β phase. For these analyses, the wavelength was 0.154036 nm (Cu Kα), the 2θ range was 30–45° and the 2θ step size was 0.05°. XRD analyses were realized for samples submitted to various heat treatment. The samples were set into the furnace once the studied temperature is reached, maintain for a given time and cooled down on a refractory brick.

3. Constitutive model and numerical methods

3.1. Constitutive model for the high temperature behavior of the Ti-6Al-4V alloy

3.1.1. Creep tests results

During the primary stage, strain hardening causes the strain rate to decrease. Then, during the secondary stage, an equilibrium between strain hardening and recovery is established, which leads to a constant strain rate. Finally, during the tertiary stage, damage leads to the final fracture of the specimen [20,21]. At high temperatures ($\geq$ 773 K), the experimental results indicate that secondary creep is predominant, with almost no primary creep. Indeed, at high temperature, the equilibrium is quickly established, and the primary creep is brief. On the other hand, at the lowest temperature (723 K), a short primary stage remains and has not been considered in this study. This work focuses on the behavior of the studied material during an industrial heat treatment, which are generally maintained at high temperature (973 K) for 2 h. In that sense, the primary stage can be neglected compared to the secondary one.

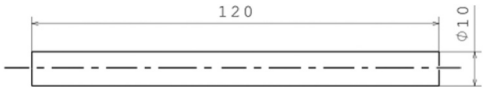

Fig. 4. Compression creep test specimen.

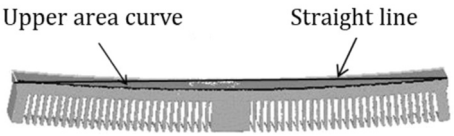

Fig. 5. Scanned cantilever.

For both tension and compression, the steady creep strain rate $\dot{\varepsilon}$ has been determined for each test with the least square method. These results are plotted and compared to each other in Fig. 8. The error bar is based on the standard deviation calculated for each configuration. Whatever the temperature is, the behavior is symmetrical in the studied range of pressure, which means that the effect of the hydrostatic pressure is not significant in the range of interest. This can be interpreted by the fact that the applied hydrostatic pressure is not sufficient to close pores. Moreover, for each temperature a power law has been fitted and plotted to show that these functions seem to fit the experimental results. It should be noticed that, for confidentiality purposes, the experimental results of this current work have been normalized by the maximum applied stress during the creep tests (σ_{ref}) and by the maximum strain rate obtained for these tests ($\dot{\varepsilon}_{ref}$).

3.1.2. Model description and material parameters

In order to model the high temperature behavior of the SLM produced Ti-6Al-4V alloy, and according to the results presented in Fig. 8, a power law relation, which includes an Arrhenius term for the temperature dependence, is used:

$$\dot{\varepsilon}_c[\sigma, \mathrm{T}] = A\sigma^{1/m[T]}\exp\left(-\frac{Q[\mathrm{T}]}{RT}\right) \tag{1}$$

In the above relation, which has been used by Yan et al. [9] to describe the viscoplastic behavior of conventional Ti-6Al-4V during a post-welding heat treatment, σ is the equivalent stress while A, m and Q are some parameters. Specifically, m is the strain-rate sensitivity coefficient and Q is the activation energy. In this study, because material properties are considered isotropic, the equivalent stress is defined according to the definition of von Mises. As discussed in the following section, some important microstructural transformations are observed during heat treatments depending on the prescribed temperature, essentially because the initial microstructure represents a state which is away from thermodynamic equilibrium. The direct consequence is that, in contrast with the work of Yan et al. [9], the parameters m and Q need to be temperature-dependent for the viscoplastic behavior to be correctly described.

In order to identify the material parameters, the following strategy has been adopted. First, based on the results given in Fig. 8, the strain rate sensitivity coefficient m has been estimated for each temperature with a power law ($\dot{\varepsilon} = \sigma^{1/m[T]}$) and the least-square method. According to the results (see Fig. 9), the strain rate sensitivity coefficient increases with an increasing temperature. Also, there is a significant change of slope around 873 K, which is likely due to microstructure evolution. Interestingly, at high temperatures ($>$ 873 K), the strain rate sensitivity coefficient reaches a value that is similar to that obtained for the α + β microstructure [12,22]. As suggested by the experimental results, the temperature dependence of m is modeled with two affine functions (see

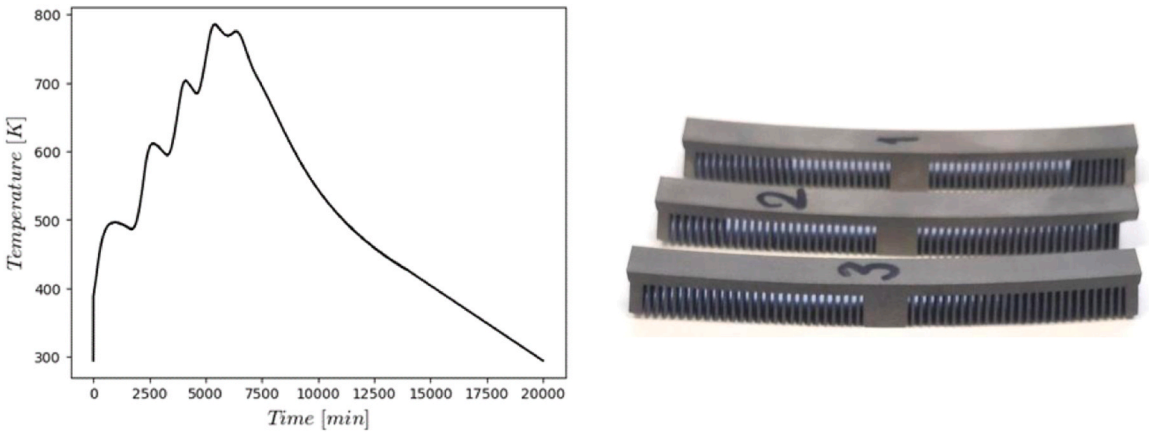

Fig. 6. Temperature evolution for the heat treatment 1 (left) and corresponding distorted cantilevers (right).

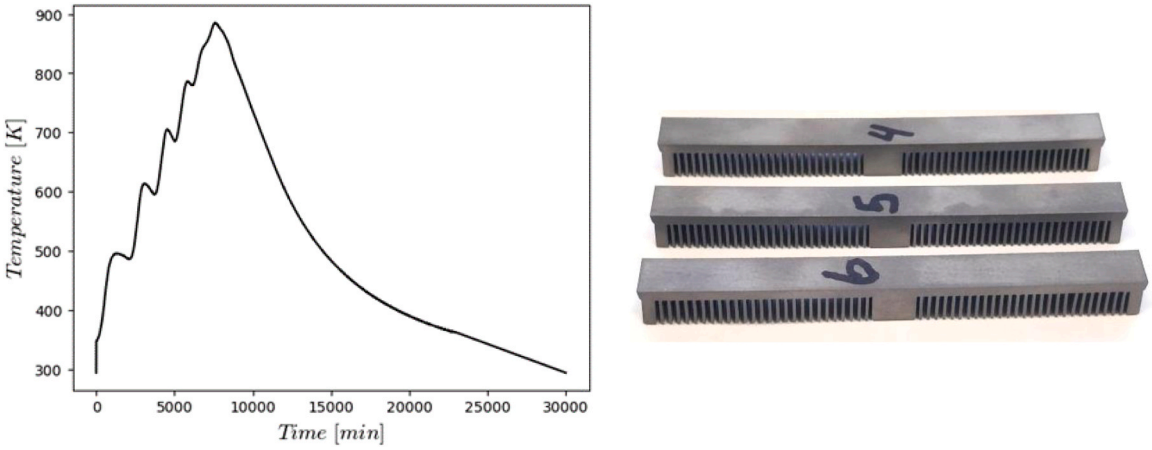

Fig. 7. Temperature evolution for the heat treatment 2 (left) and corresponding distorted cantilevers (right).

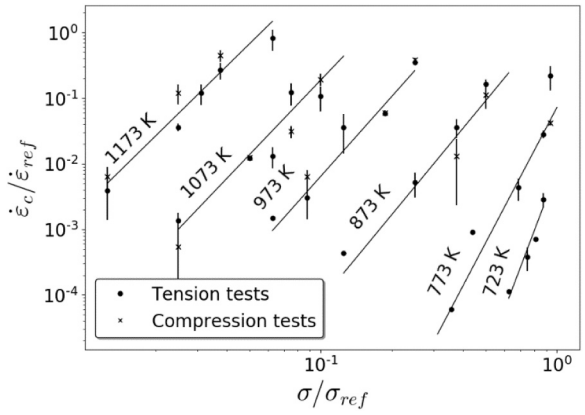

Fig. 8. Evolution of the dimensionless strain rate as a function of the dimensionless stress. The points represent the creep tests results. The lines represent the identified creep model for each temperature.

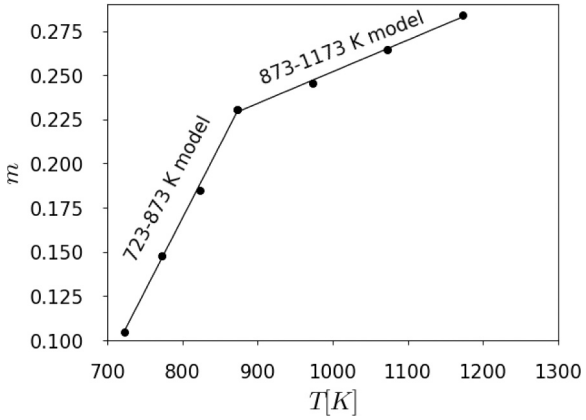

Fig. 9. Evolution of the strain rate sensitivity coefficient m as a function of the temperature. The points are the identified values from each tested temperature. The solid lines represent the model of the strain rate sensitivity coefficient identified with the points.

Eq. (2)) with a transition temperature of 873 K (Fig. 9).

$$m[T] = \begin{cases} 8.278000 \times 10^{-4} T - 4.936594, & T \leq 873K \\ 1.800000 \times 10^{-4} T + 7.196000 \quad , & T \geq 873K \end{cases} \tag{2}$$

It is emphasized that the function *m[T]* is continuous in the sense that both affine functions provide the same m value for 873 K. Second, to determine the temperature dependent material parameters *Q[T]* and the constant A, the parameter *B[T]* has been calculated according to:

$$B[T] = \frac{\dot{\varepsilon}_c[\sigma, \mathrm{T}]}{\sigma^{\frac{1}{m[T]}}} = A \exp\left(-\frac{Q[\mathrm{T}]}{RT}\right) \tag{3}$$

The variable $B[T]$ is plotted as a function of $1/T$ with a log-log scale in Fig. 10. This data has been used to determine the parameters A and *Q[T]*.

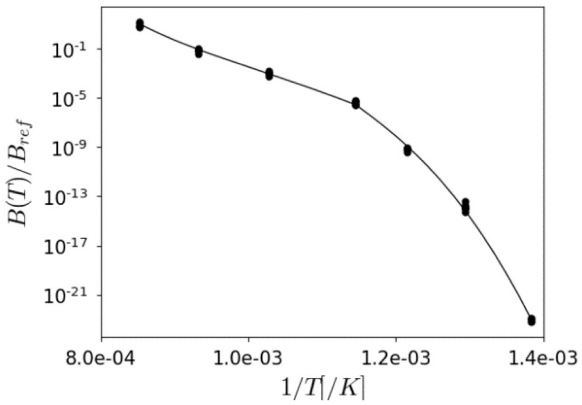

Fig. 10. Evolution of the parameter B[T] as a function of the inverse of the temperature. The points are the identified values from each tested temperature. The solid lines represent the model of B[T] = f[1/T] identified with the points. B is defined as B[T] = Aexp(−Q[T]/RT).

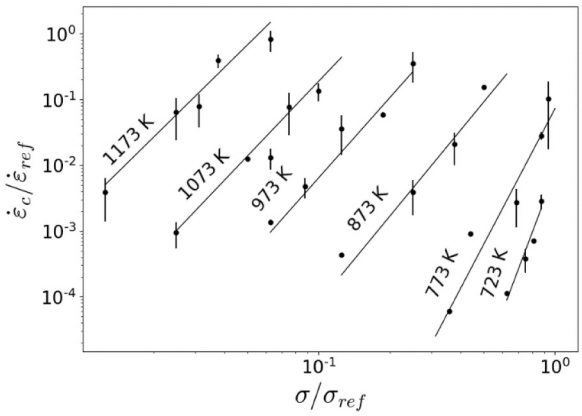

Fig. 12. Evolution of the dimensionless strain rate as a function of the dimensionless stress. The points represent the creep tests results. The solid lines represent the identified creep model for each temperature.

To correctly reproduce the temperature-dependence of $B[T]$, the activation energy function *Q[T]* has been defined with two polynomial functions to consider the impact of the absolute temperature. Specifically, the first polynomial function allows considering the evolution of *Q[T]* from 723 K to 873 K while the second polynomial function applies from 873 K to 1073 K. The different coefficients of these polynomial functions and the constant *A* have been optimized so that the difference between the model and the experimental values for $B[T]$ is minimal for all temperatures. The corresponding activation energy function *Q[T]* is shown in Fig. 11. It should be noted that B_{ref} is the maximal value of *B [T]*, obtained from the tests.

The corresponding activation energy function *Q[T]* is shown in Fig. 11. It should be noticed that, at high temperatures (T ≥ 973 K), the activation energy is comparable to that of self-diffusion for titanium found in the literature: 236 kJ/mol [23], 273 kJ/mol [24] and 303 kJ/mol [25].

The stationary creep strain rate calculated with the proposed creep model is compared to the experimental data in Fig. 12. The experimental data gathers both tension and compression tests. According to the results, the agreement with the experimental data is generally correct, the average relative error being about 36%.

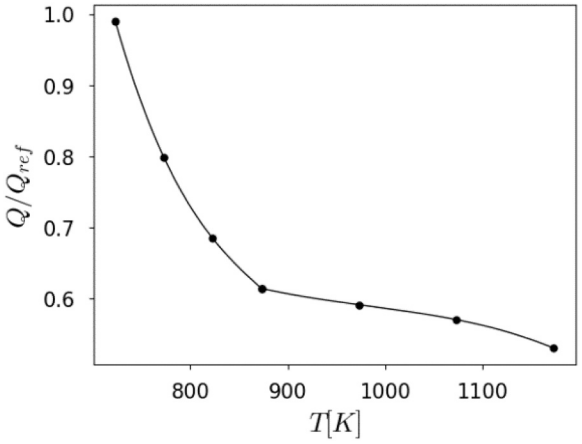

Fig. 11. Evolution of the activation energy Q as function of the temperature. The points are the identified values for each temperature. The solid lines represent the model identified with the points.

3.2. Numerical model of the cantilever

The identified constitutive model of the previous section has been used in the numerical simulation of the cantilever. This simulation specifications are presented in this section.

The simulation of the printing and the heat treatment of the cantilevers have been performed with the commercial FEM software ABAQUS®. To reduce the computation time, only a quarter of the part has been considered by taking advantages of the two symmetry planes. The elements used were 8 nodes linear bricks with reduced integration (C3D8R). Their size was about 0.1 mm along the printing direction (Z) and 0.3 mm in the other directions (X and Y). To simulate the printing operation, the inherent strain method has been used [31]. The eigenstrain tensor used for the application of this method has been calibrated and validated in a previous work [32]. Then, the heat treatment is performed with a transient quasi-static step. The set of constitutive relations includes temperature dependent material properties: the elastic properties were taken from the JMatPro© software and are similar to literature data [33–35]. Also, a creep subroutine was scripted with the identified creep model, presented in the previous section. During the simulation of this heat treatment, the temperature was considered homogeneous inside the part. This means that the temperature evolution is directly controlled on each node of the mesh with no heat conduction. To ensure that this assumption is reasonable, some preliminary simulations, that include heat conduction, have been carried out. The temperature evolution used for the numerical simulation is the one measured during the heat treatments (see Figs. 6 and 7). As shown in Fig. 14, the baseplate is also taken into account and tied to the cantilever. Indeed, the top nodes from the baseplate and the bottom nodes from the cantilever are tied together. As mentioned previously two symmetry constraints are imposed on all nodes of the symmetry planes.

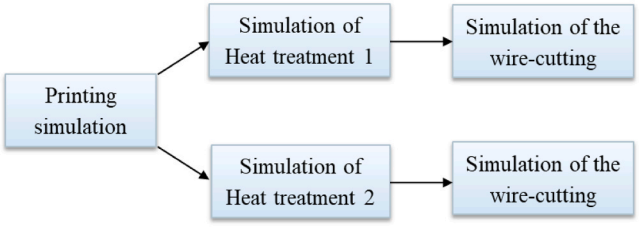

Fig. 13. Flowchart of the different steps of the simulation.

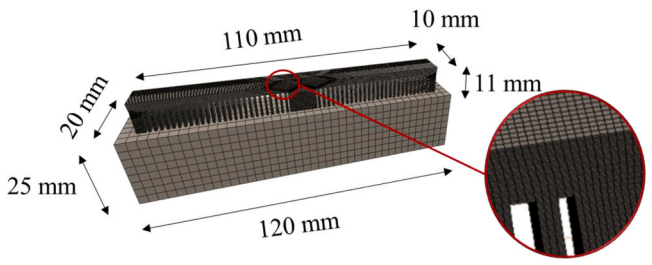

Fig. 14. Cantilever mesh.

Table 1
Distortion results for heat treatment 1 and 2.

	Heat treatment 1			Heat treatment 2		
Cantilevers	1	2	3	4	5	6
Maximal deflection (mm)	2,62	2,71	2,67	0,57	0,60	0,57
Average of maximal deflections (mm)	2,65			0,58		

Moreover, the node belonging to both the bottom face of the baseplate and the symmetry planes has its degrees of freedom blocked in all three directions. Only a part of the baseplate is represented in the simulation. Finally, the wire cutting stage has been simulated by the removal of the baseplate and by applying isostatic boundary conditions on the cantilever. In other words, the elements belonging to the baseplate have been deactivated and the tie constraints deleted. The two boundary conditions on the symmetry planes remain, and the node at the intersection of these planes with the baseplate is blocked in all directions. Fig. 13 shows the different simulation steps realized in this study.

4. Results

4.1. Experimental results

In order to compare the experimental and numerical results, the maximum vertical deflection has been determined for each cantilever (Fig. 5). The experimentally determined deflections are presented in Table 1. According to the results, the first treatment leads to higher deflections. This is likely due to the fact that the prescribed temperature of 773 K is not sufficient for residual stresses to be significantly relaxed, which causes distortions during cutting operations.

4.2. Numerical results

As presented in Section 3.2, the simulation sequence consists of the printing stage, the partial heat treatment and the cutting from the baseplate. The resulting geometries are presented in Fig. 15, where the vertical displacement fields obtained for both heat treatments are displayed.

4.3. Comparison

The average experimental deflections have been calculated for each heat treatment and compared to the simulation results in Table 2. The experimental and numerical vertical distortions are plotted in Fig. 16 for both heat treatments. According to the results, and considering the experimental error (measurement technique, roughness of the surface, wire-cutting) is about 0.1 mm, the agreement between experiment and simulation is generally acceptable for industrial applications. The absolute errors for both heat treatments are negligible, which means that the proposed constitutive model provides a reasonable description of the high temperature behavior of the SLM produced Ti-6Al-4V alloy.

5. Industrial application

This section deals with the application of the identified creep model on an industrial build. For illustration purposes, the geometry of this industrial component, known as Xfitting, is first presented. The experimental procedure and numerical model are explained in the next paragraphs, and the calculated distortions are compared to the experiment.

The Xfitting part is a bracket designed for the AIRBUS® A350 airplane. The small size of this part (cf. Fig. 17) allows printing four of them in a single build.

5.1. Experimental procedure

The nesting of the four Xfitting parts has been printed with the M2 Concept Laser machine. After printing, the nesting has been heat treated with an industrial heat treatment, for which the prescribed temperature is given in Fig. 18. This industrial heat treatment consists in a slow heating up to 993 K, a holding stage for 2 h and a slow cooling. All the Xfitting parts have then been removed from the baseplate and supports via electric discharge machining. It should be noted that multiple 3D

Table 2
Comparison between numerical and experimental deflections of the cantilevers.

	Heat treatment 1	Heat treatment 2
Experimental deflection (mm)	2,65	0,58
Numerical deflection (mm)	2,34	0,71
Absolute error (mm)	0,31	0,13

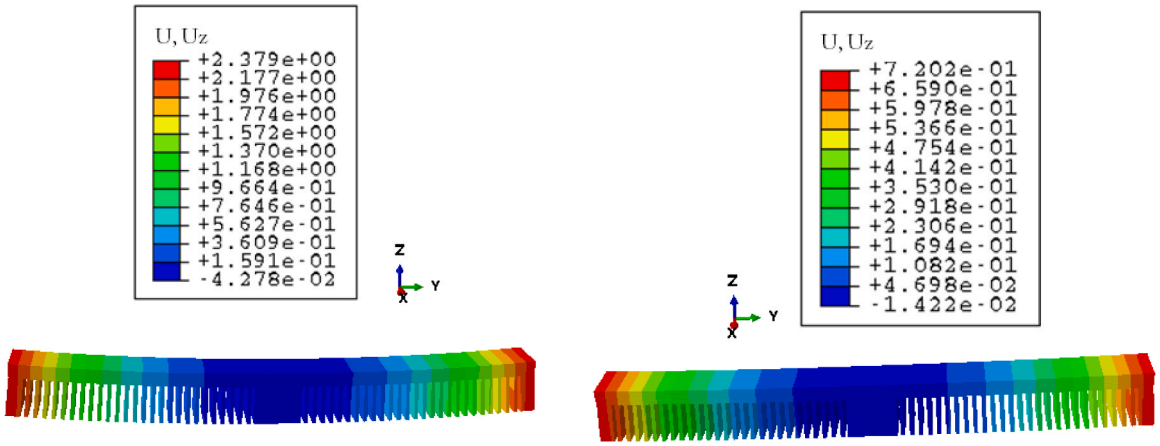

Fig. 15. Displacement Uz for heat treatment 1 (left) and 2 (right).

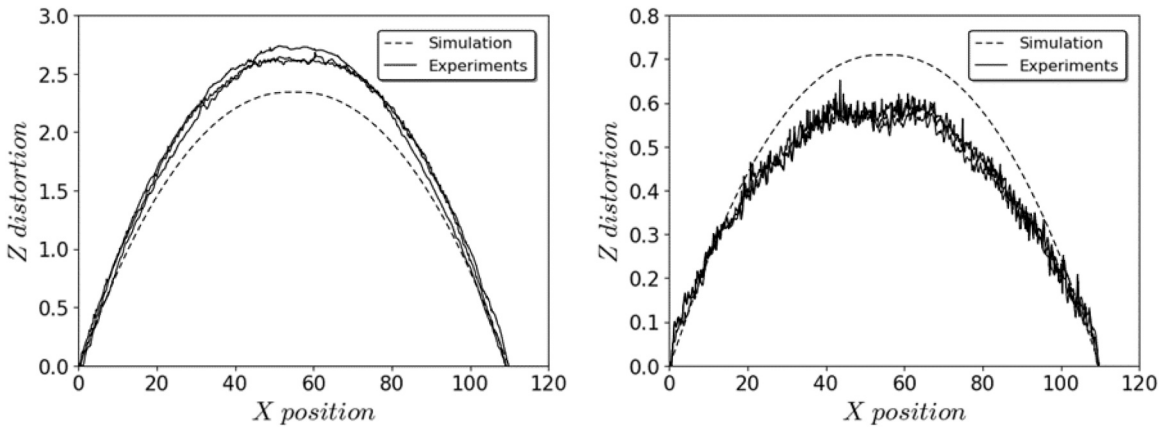

Fig. 16. Comparison between numerical and experimental distortions of the cantilevers for heat treatment 1 (left) and heat treatment 2 (right).

scans have been realized at different stages to understand how the distortions are impacted by the process. The 3D scans have been performed with a Creaform Handyscan 700® after printing and after cutting.

5.2. Numerical model

As before, the ABAQUS® FEM solver has been used for the simulation of the heat treatment. In the Finite Element model, the Xfitting and the beam supports are meshed with 1 mm tetrahedral elements (C3D4). The wafer supports, which have a thickness of 300 μm, are assimilated as 1 mm thick shell elements with reduced integration (S3R). The baseplate is meshed with 4 mm brick elements with reduced integration (C3D8R). Four Xfitting parts are printed in one build (cf. Fig. 19), the supports are tied to the Xfitting parts and both Xfitting parts and supports are tied to the top face of the baseplate.

The simulation of the printing operation has been performed with the inherent strain method [32]. For the heat treatment, isostatic boundary conditions are applied on the baseplate. The heat treatment analysis has been realized as a transient quasi-static step and the material behavior is described with the proposed constitutive model. The constitutive model also considers the temperature dependence of mass density, thermal expansion and stiffness properties. During the heat treatment simulation, the temperature is considered homogeneous. The amplitude applied on the model corresponds to the one measured in the furnace (cf. Fig. 18). Finally, at the end of the heat treatment the support removal is simulated for each Xfitting part by deleting the supports, the baseplate and the other Xfitting parts and applying isostatic boundary conditions. In this case, the boundary conditions are applied to 3 nodes to carry the part without introducing rigid body movements or create new constraints (cf. Fig. 19).

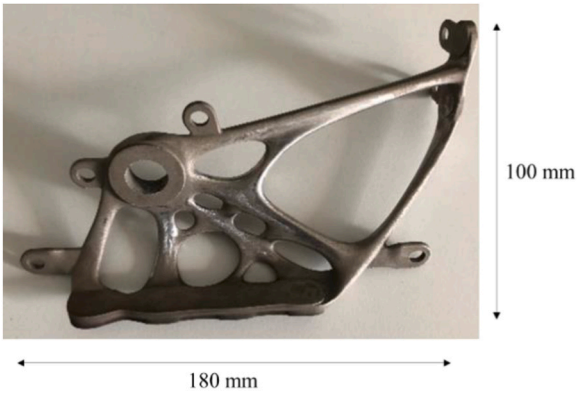

Fig. 17. One of the Xfitting parts after support removal.

5.3. Comparison

In the following, only one Xfitting part among four is considered for the comparison with experimental results. To discuss the possible discrepancies between numerical and experimental results, it is necessary to compare the geometries obtained after printing and after cutting. Because the corresponding orientations are not the same, the post-printing and post-cutting geometries have first been adjusted using a best fit algorithm, available in the GOM Inspect software. To determine the distortions resulting from the heat treatment and cutting operations, the geometry after support removal has been projected (orthogonal projection) onto the one measured after printing. This strategy for the determination of distortions has been applied on both the experimental and numerical geometries (cf. Fig. 20 and 21). A negative distortion means that the geometry after support removal is beneath the one after printing, a positive value means the opposite.

As illustrated by Fig. 20 and 21, the simulation results and the 3D scans are in good agreement. Specifically, the maximum difference between numerical and experimental distortions is about 0.14 mm. This value is in the same order of magnitude that the accuracy of 3D scans, which is about 0.1 mm. Such results indicate that the proposed method for evaluating distortions can be applied to geometrically complex parts.

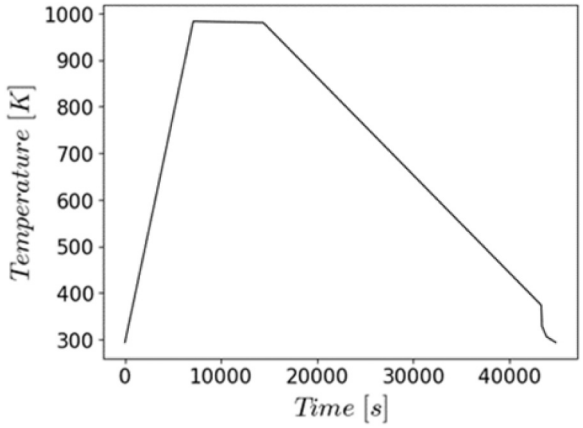

Fig. 18. Temperature evolution for the heat treatment applied to the Xfitting nesting.

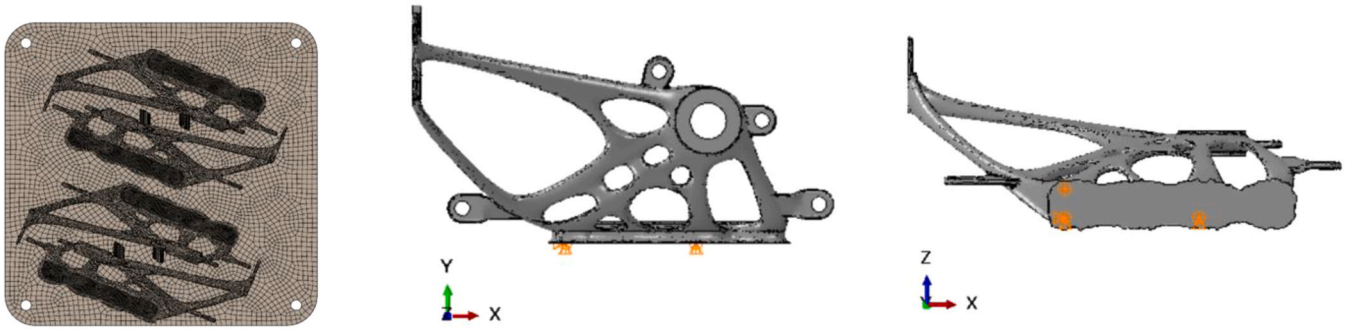

Fig. 19. Mesh of the nesting (left) and boundary conditions for the wire-cut step (right). The orange cones are the blocked degree of freedom. (For interpretation of the references to color in this figure legend, the reader is referred to the web version of this article.)

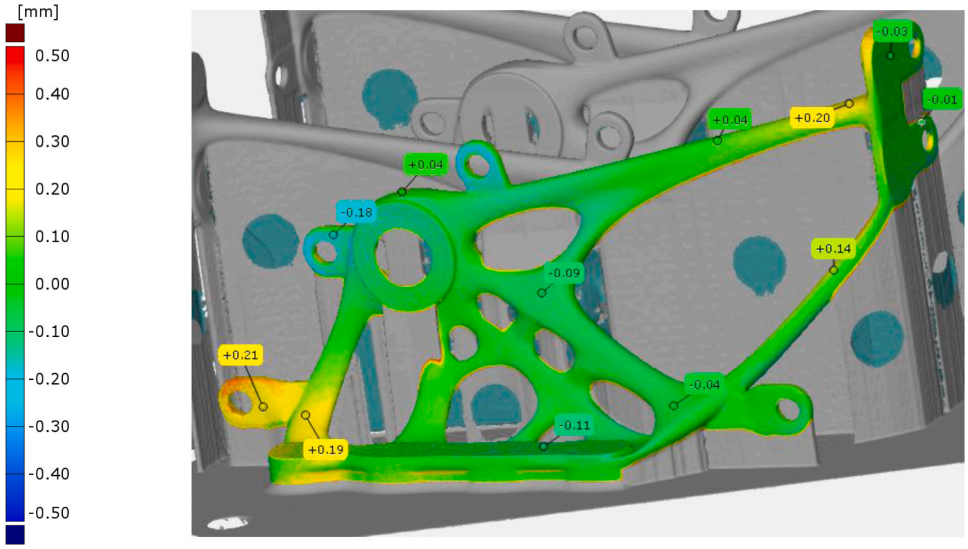

Fig. 20. Experimental distortions arising from heat treatment in one Xfitting.

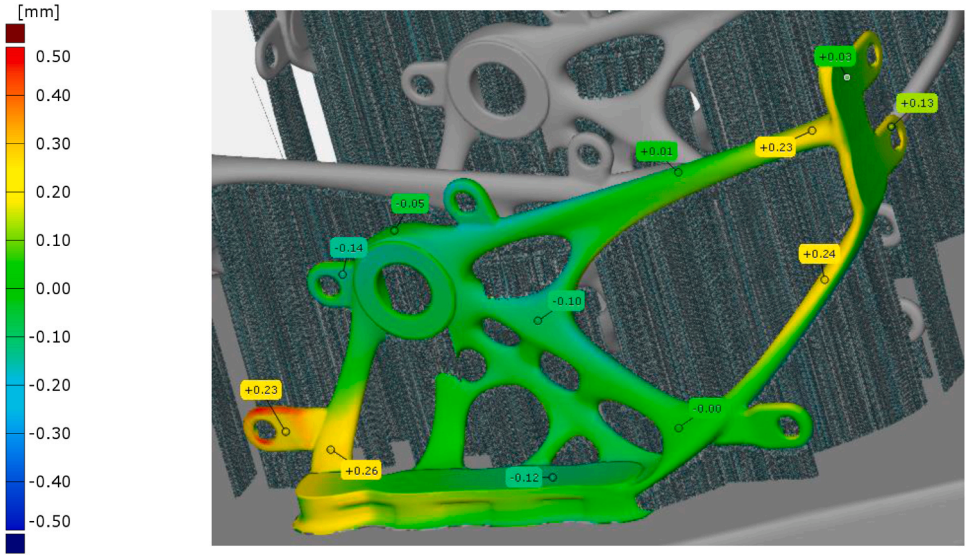

Fig. 21. Numerical distortions arising from heat treatment in one Xfitting.

6. Discussion

The constitutive model identified in the Section 3.1 showed a change of behavior around 873 K. In this section the microstructure evolution according to the temperature is discussed.

According to metallographic observations (Fig. 22), microstructural transformations strongly depend on the prescribed temperature. Indeed, as shown in Fig. 22a, for the minimum temperature (723 K), the

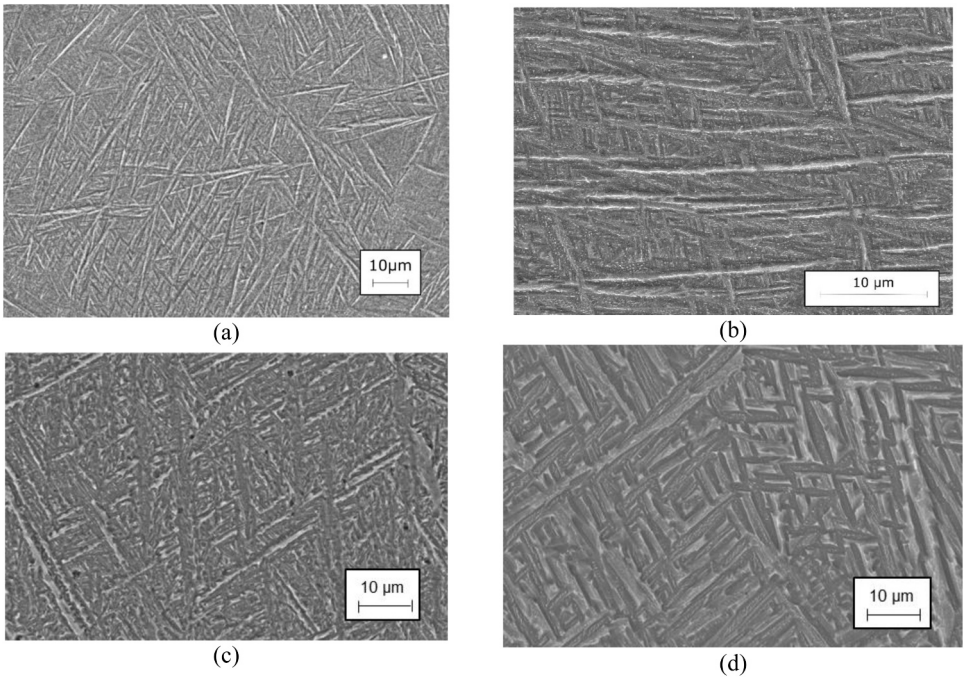

Fig. 22. Microstructure after heat treatments at 723 K 2 h (a), 973 K 30 min (b), 1073 K 30 min (c) and 1173 K for 30 min (d).

microstructure has not changed with respect to the initial α' martensitic microstructure (see Fig. 2). After treatment at 1173 K for 30 min, the martensitic phase has been totally transformed into the equilibrium α and β phases. The resulting microstructure consists of 1–3 µm thick α lamellae being embedded in a β matrix (see Fig. 22d). Fig. 22b and c show that, at intermediate temperatures (973 K and 1073 K), the decomposition of the martensitic microstructure is incomplete, and the microstructure is finer than the one obtained at 1173 K. It should be noted that similar conclusions can be found in the literature dedicated to the evolution of the microstructure during post-welding [26] or post-printing [27,14,10] heat treatments. Particularly, Wu et al. [28] indicate that, after a heat treatment below 873 K, the microstructure displays no difference with that of the as-built specimen. Then, between 873 K and 1173 K, the martensite decomposes into fine platelets. Finally, at higher temperature (between 1173 K and 1263 K), the acicular microstructure is completely transformed into platelets.

XRD analyses have also been carried out on various samples to detect the appearance of the β phase. Some samples were submitted to different temperatures for a fixed holding time of 45 min (Fig. 23) and others at a fixed temperature of 873 K for 2 different holding times (Fig. 24). As the

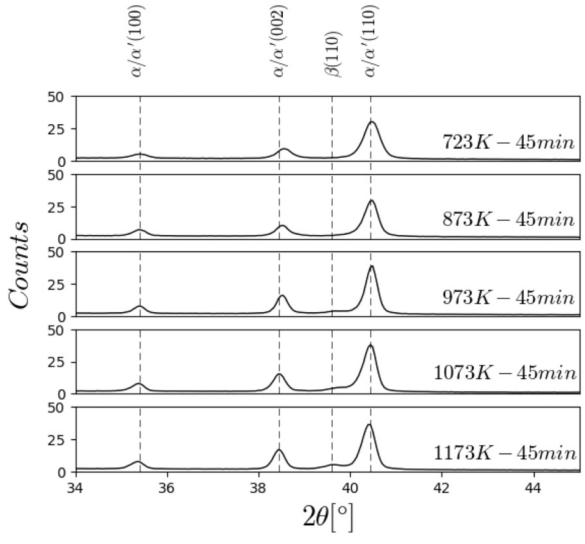

Fig. 23. Diffraction patterns for the SLM produced Ti-6Al-4V alloy after heat treatment at various temperatures between 723 K and 1173 K for 45 min.

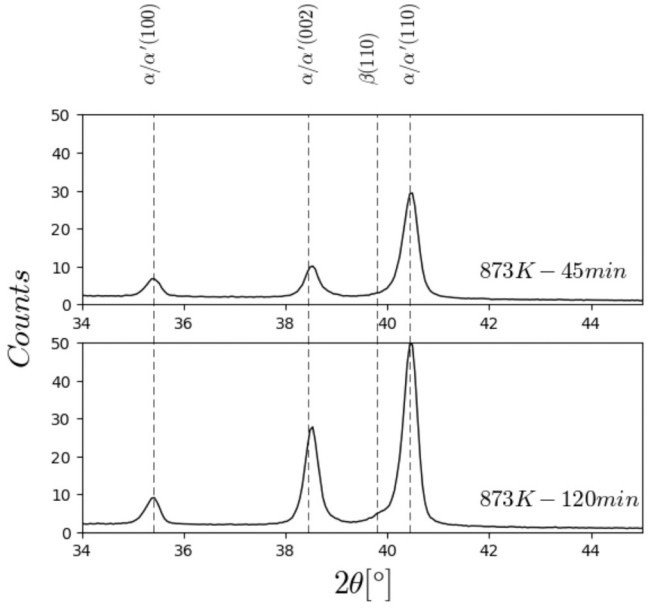

Fig. 24. Diffraction patterns for the SLM produced Ti-6Al-4V alloy after heat treatment at various holding times for 873 K.

martensitic α' phase and the α phase have the same crystal structure and very similar lattice parameters, it is not possible to differentiate one from the other from XRD results. For a holding time of 45 min, the {110} β peak, whose 2θ position is about 39.5°, is observed from 973 K. At 873 K, the same peak is observed only for the maximum holding time of 2 h. It is worth noticing that creep tests at 873 K last from few minutes to a hundred of minutes. As a result, the creep behavior should be impacted by the precipitation of the β phase from 873 K, which is also the transition temperature for the strain rate sensitivity coefficient m. The progressive evolution of the creep behavior can therefore be interpreted as the macroscopic effect of the dissolution of the martensitic phase α'. The present results are consistent with those of Yang et al. [29] who detected a β peak for a sample that has been heat treated at 908 K for 90 min. Moreover, Xu et al. [30] studied the martensite decomposition by looking at the variation of the Vanadium content. They concluded that the most of the β laths are formed at the range temperature of 873–1123 K. This result is in line with the previous observations made in this section.

7. Conclusions

In this study, a strategy for the simulation of the stress relief heat treatment applied to SLM produced Ti-6Al-4V parts has been proposed. For this purpose, different creep tests have been performed at temperatures ranging from 723 K to 1173 K. According to the results, the stationary creep strain rate is independent on the hydrostatic pressure, which indicates that the high temperature behavior is not impacted by the initial porosity in the investigated range. The experimental dataset has then been used to identify the material parameters of a viscoplastic constitutive model. The material parameters are observed to change significantly from 873 K. According to metallographic observations, this change is due to the progressive transformation of the initial martensitic α' microstructure into the two phases $\alpha + \beta$ lamellar microstructure.

To validate the proposed approach, some numerical simulations have been performed for two different heat treatments, for which distortions have been measured. Then, an application of an industrial part is also presented. For both parts, numerical and experimental distortions have been compared to each other. Finally, the agreement between experimental and numerical data is correct. The proposed strategy could thus be used to optimize processing conditions in order to limit distortions and control residual stresses. Future work will focus on the simulation of the Hot Isostatic Pressing (HIP) that is applied after heat treatment. This stage, which aims at closing pores, requires high hydrostatic pressures. Some specific developments will therefore be needed to consider the spherical strains resulting from the pore closure phenomenon.

CRediT authorship contribution statement

Amandine Cardon: Investigation, Validation, Writing. **Charles Mareau**: Supervision, Validation. **Yessine Ayed**: Supervision, Validation. **Sjoerd Van der Veen**: Supervision, Project administration, Validation. **Eliane Giraud**: Validation. **Philippe Dal Santo**: Supervision, Validation.

Declaration of Competing Interest

The authors declare that they have no known competing financial interests or personal relationships that could have appeared to influence the work reported in this paper.

Acknowledgement

The author would like to thank Airbus Operations SAS®, AMValor® and Airbus APWorks® for its support during this investigation.

References

[1] J.P. Kruth, L. Froyen, J. Van Vaerenbergh, P. Mercelis, M. Rombouts, B. Lauwers, Selective laser melting of iron-based powder, J. Mater. Process. Technol. 149 (1–3) (2004) 616–622, https://doi.org/10.1016/j.jmatprotec.2003.11.051.
[2] P. Li, D.H. Warner, A. Fatemi, N. Phan, Critical assessment of the fatigue performance of additively manufactured Ti–6Al–4V and perspective for future research, Int. J. Fatigue 85 (2016) 130–143, https://doi.org/10.1016/j.ijfatigue.2015.12.003.
[3] I. Setien, M. Chiumenti, S. Van Der Veen, M. San Sebastian, F. Garciandía, A. Echeverría, Empirical methodology to determine inherent strains in additive manufacturing, Comput. Math. Appl. 78 (2019) 2282–2295, https://doi.org/10.1016/j.camwa.2018.05.015.
[4] Z. Zhou, S. Bhamare, G. Ramakrishnan, S.R. Mannava, K. Langer, Y. Wen, D. Qian, V.K. Vasudevan, Thermal relaxation of residual stress in laser shock peened Ti–6Al–4V alloy, Surf. Coat. Technol. 206 (22) (2012) 4619–4627, https://doi.org/10.1016/j.surfcoat.2012.05.022.
[5] Y. Zong, P. Liu, B. Guo, D. Shan, Investigation on high temperature short-term creep and stress relaxation of titanium alloy, Mater. Sci. Eng. A 620 (2015) 172–180, https://doi.org/10.1016/j.msea.2014.10.015.
[6] P. Liu, Y. Zong, D. Shan, B. Guo, Relationship between constant-load creep, decreasing-load creep and stress relaxation of titanium alloy, Mater. Sci. Eng. A 638 (2015) 106–113, https://doi.org/10.1016/j.msea.2015.04.054.
[7] X. Cui, X. Wu, M. Wan, B. Ma, Y. Zhang, A novel constitutive model for stress relaxation of Ti-6Al-4V alloy sheet, Int. J. Mech. Sci. 161–162 (2019), 105034, https://doi.org/10.1016/j.ijmecsci.2019.105034.
[8] J. Xiao, D. Li, X. Li, et al., Modeling and simulation for the stress relaxation behavior of Ti-6Al-4V at medium temperature, Rare Met. Mater. Eng. 44 (5) (2015).
[9] G. Yan, A. Crivoi, Y. Sun, N. Maharjan, X. Song, F. Li, M.J. Tan, An Arrhenius equation-based model to predict the residual stress relief of post weld heat treatment of Ti-6Al-4V plate, J. Manuf. Process. 32 (2018) 763–772, https://doi.org/10.1016/j.jmapro.2018.04.004.
[10] A.A. Antonysamy, Microstructure, Texture and Mechanical Property Evolution during Additive Manufacturing of Ti6Al4V Alloy for Aerospace Applications.pdf, Manchester University, 2012.
[11] Z. Wang, A.D. Stoica, D. Ma, A.M. Beese, Stress relaxation behavior and mechanisms in Ti-6Al-4V determined via in situ neutron diffraction: application to additive manufacturing, Mater. Sci. Eng. A 707 (2017) 585–592, https://doi.org/10.1016/j.msea.2017.09.071.
[12] Y.-K. Kim, S.-H. Park, J.-H. Yu, B. AlMangour, K.-A. Lee, Improvement in the high-temperature creep properties via heat treatment of Ti-6Al-4V alloy manufactured by selective laser melting, Mater. Sci. Eng. A 715 (2018) 33–40, https://doi.org/10.1016/j.msea.2017.12.085.
[13] L. Thijs, F. Verhaeghe, T. Craeghs, J.V. Humbeeck, J.-P. Kruth, A study of the microstructural evolution during selective laser melting of Ti–6Al–4V, Acta Mater. 58 (9) (2010) 3303–3312, https://doi.org/10.1016/j.actamat.2010.02.004.
[14] B. Vrancken, L. Thijs, J.-P. Kruth, J. Van Humbeeck, Heat treatment of Ti6Al4V produced by Selective Laser Melting: microstructure and mechanical properties, J. Alloy. Compd. 541 (2012) 177–185, https://doi.org/10.1016/j.jallcom.2012.07.022.
[15] S. Liu, Y.C. Shin, Additive manufacturing of Ti6Al4V alloy: a review, Mater. Des. 164 (2019), 107552, https://doi.org/10.1016/j.matdes.2018.107552.
[16] G. Kasperovich, J. Hausmann, Improvement of fatigue resistance and ductility of TiAl6V4 processed by selective laser melting, J. Mater. Process. Technol. 220 (2015) 202–214, https://doi.org/10.1016/j.jmatprotec.2015.01.025.
[17] B. Wysocki, P. Maj, R. Sitek, J. Buhagiar, K. Kurzydłowski, W. Święszkowski, Laser and electron beam additive manufacturing methods of fabricating titanium bone implants, Appl. Sci. 7 (7) (2017) 657, https://doi.org/10.3390/app7070657.
[18] H.K. Rafi, N.V. Karthik, H. Gong, T.L. Starr, B.E. Stucker, Microstructures and mechanical properties of ti6al4v parts fabricated by selective laser melting and electron beam melting, J. Mater. Eng. Perform. 22 (12) (2013) 3872–3883, https://doi.org/10.1007/s11665-013-0658-0.
[19] EOS GmbH, Material data sheet EOS Titanium Ti64, 2014.
[20] F. Saint-Antonin, Essais de fluage, Tech. Ing. Essais Mécaniques Sur Métaux Alliages, 1995, p. 18.
[21] M.A. Meyers, K.K. Chawla, et al., Mechanical Behavior of Materials, p. 882, 2009.
[22] W.J. Evans, G.F. Harrison, Power law steady state creep in ?/? titanium alloys, J. Mater. Sci. 18 (1983) 3449–3455.
[23] R.I. Jaffee, H.M. Burte, et al., Titanium Science and Technology, Springer US, Boston, MA, 1973.
[24] G. Malakondaiah, N. Prasad, P. Rama Rao, On the evaluation of activation energy for viscous creep through temperature change tests, Scr. Metall. 16 (4) (1982) 421–426, https://doi.org/10.1016/0036-9748(82)90165-X.
[25] M. Köppers, C. Herzig, Y. Friesel, M. Mishin, Intrinsic self-diffusion and substitutional Al diffusion in alpha-Ti, Acta Mater. 45 (1997) 4181–4192.
[26] T. Ahmed, H.J. Rack, Phase transformations during cooling in α+ β titanium alloys, Mater. Sci. Eng. A 243 (1) (1998) 206–211.
[27] L.E. Murr, S.A. Quinones, S.M. Gaytan, M.I. Lopez, A. Rodela, E.Y. Martinez, D. H. Hernandez, E. Martinez, F. Medina, R.B. Wicker, Microstructure and mechanical behavior of Ti–6Al–4V produced by rapid-layer manufacturing, for biomedical applications, J. Mech. Behav. Biomed. Mater. 2 (1) (2009) 20–32, https://doi.org/10.1016/j.jmbbm.2008.05.004.
[28] S.Q. Wu, Y.J. Lu, Y.L. Gan, T.T. Huang, C.Q. Zhao, J.J. Lin, S. Guo, J.X. Lin, Microstructural evolution and microhardness of a selective-laser-melted Ti–6Al–4V

alloy after post heat treatments, J. Alloy. Compd. 672 (2016) 643–652, https://doi.org/10.1016/j.jallcom.2016.02.183.
[29] Y. Yang, Y.J. liu, J. Chen, H.L. Wang, Z.Q. Zhang, Y.J. Lu, S.Q. Wu, J.X. Lin, Crystallographic features of α variants and β phase for Ti-6Al-4V alloy fabricated by selective laser melting, Mater. Sci. Eng. A 707 (2017) 548–558, https://doi.org/10.1016/j.msea.2017.09.068.
[30] W. Xu, E.W. Lui, A. Pateras, M. Qian, M. Brandt, In situ tailoring microstructure in additively manufactured Ti-6Al-4V for superior mechanical performance, Acta Mater. 125 (2017) 390–400, https://doi.org/10.1016/j.actamat.2016.12.027.
[31] M.G. Yuan, Y. Ueda, Prediction of residual stresses in welded T-and I-joints using inherent strains, J. Eng. Mater. Technol. Trans. ASME 2 (118) (1996) 229–234.
[32] B. Ahmad, S.O. van der Veen, M.E. Fitzpatrick, H. Guo, Residual stress evaluation in selective-laser-melting additively manufactured titanium (Ti-6Al-4V) and inconel 718 using the contour method and numerical simulation, Addit. Manuf. 22 (2018) 571–582, https://doi.org/10.1016/j.addma.2018.06.002.
[33] C. Ramirez, Crières d'optimisation des alliages de Titane pour améliorer leur usinabilité, École Nationale Supérieure d'Arts et Métiers, 2009.
[34] M. Surand, Étude du comportement viscoplastique en traction et en fluage de l'alliage TA6V de 20 à 600 degrés Celsius, 2013.
[35] A. Krishnakumar, K. Suresh, A. Chandrasekar, et al., Towards Assembly-Free Methods for Additive Manufacturing Simulation, présenté à ASME 2015 International Design Engineering Technical Conferences and Computers and Information in Engineering Conference, Boston, Massachusetts, USA, 2015, doi: 10.1115/DETC2015–46356.